ChemBioChem

Supporting Information

Molecular Basis of the Antiangiogenic Action of Rosmarinic Acid, a Natural Compound Targeting Fibroblast Growth Factor-2/FGFR Interactions

Katiuscia Pagano,* Laura Carminati, Simona Tomaselli, Henriette Molinari, Giulia Taraboletti, and Laura Ragona*

Supporting Information

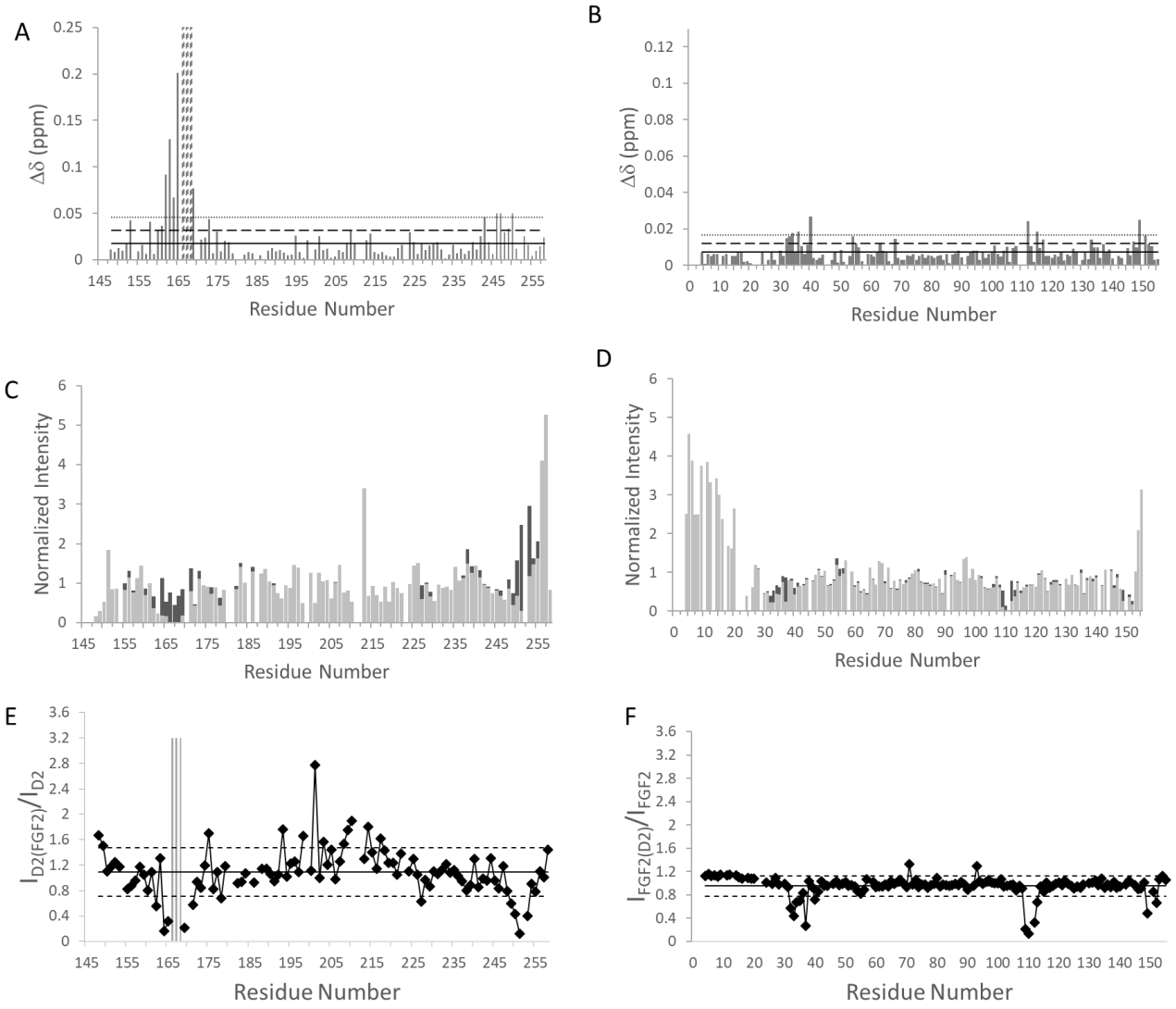

Figure S1. Chemical shift perturbations and cross peak intensity changes upon FGF2/FGFR-D2 complex formation. Experiments were acquired on 0.26mM proteins, at ^{15}N-FGF2:^{15}N-FGFR-D2 1:1 molar ratio, pH = 6.5, at 25 °C at 600 MHz. Chemical shift perturbations are shown for FGFR-FGFR-D2 and FGF2 in A and B, respectively. Continuous, dashed, and dotted lines represent the CSP average values (⟨CSP⟩), ⟨CSP⟩ + 1σ, and ⟨CSP⟩ + 2σ, respectively. Dashed vertical bars represent residues whose intensities broaden beyond detection upon complex formation. C) FGFR-D2 normalized intensities in the absence (black bars) and in the presence of FGF2 (grey bars). D) FGF2 normalized intensities in the absence (black bars) and in the presence of FGFR-D2 (grey bars). Intensity ratios of FGFR-D2 (E) and FGF2 (F) upon formation of the FGFR-D2/FGF2 complex. Straight and dotted lines represent the average and the average ± 1σ, respectively. Grey vertical bars in F) represent residues whose intensity broadens beyond detection upon complex formation.

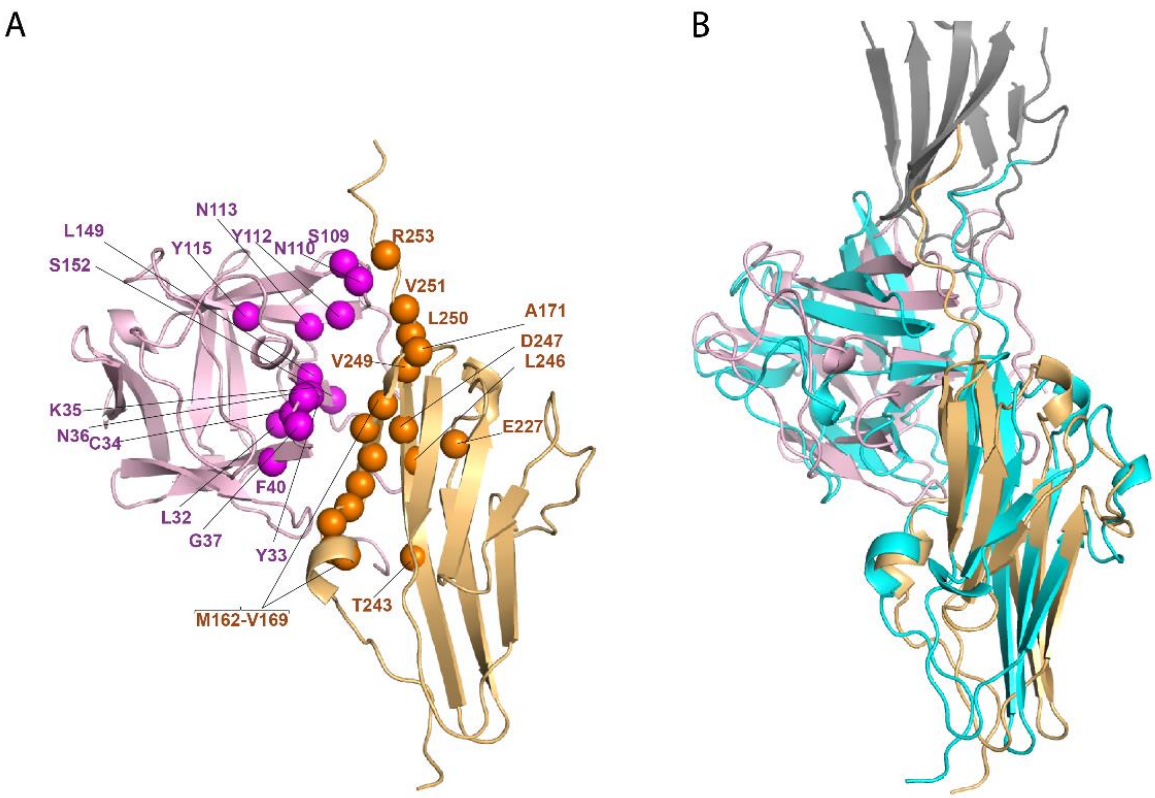

Figure S2. Docked model of FGF2/FGFR-D2 complex. A) Representative structure of FGF2 (pink)/FGFR-D2 (orange) complex (cluster 2) obtained with Haddock. Residues defined as active residues in the Haddock calculations are shown as spheres on the structures. B) The docked model was aligned with the crystallographic structure (PDB id: 1ev2, cyan and grey).

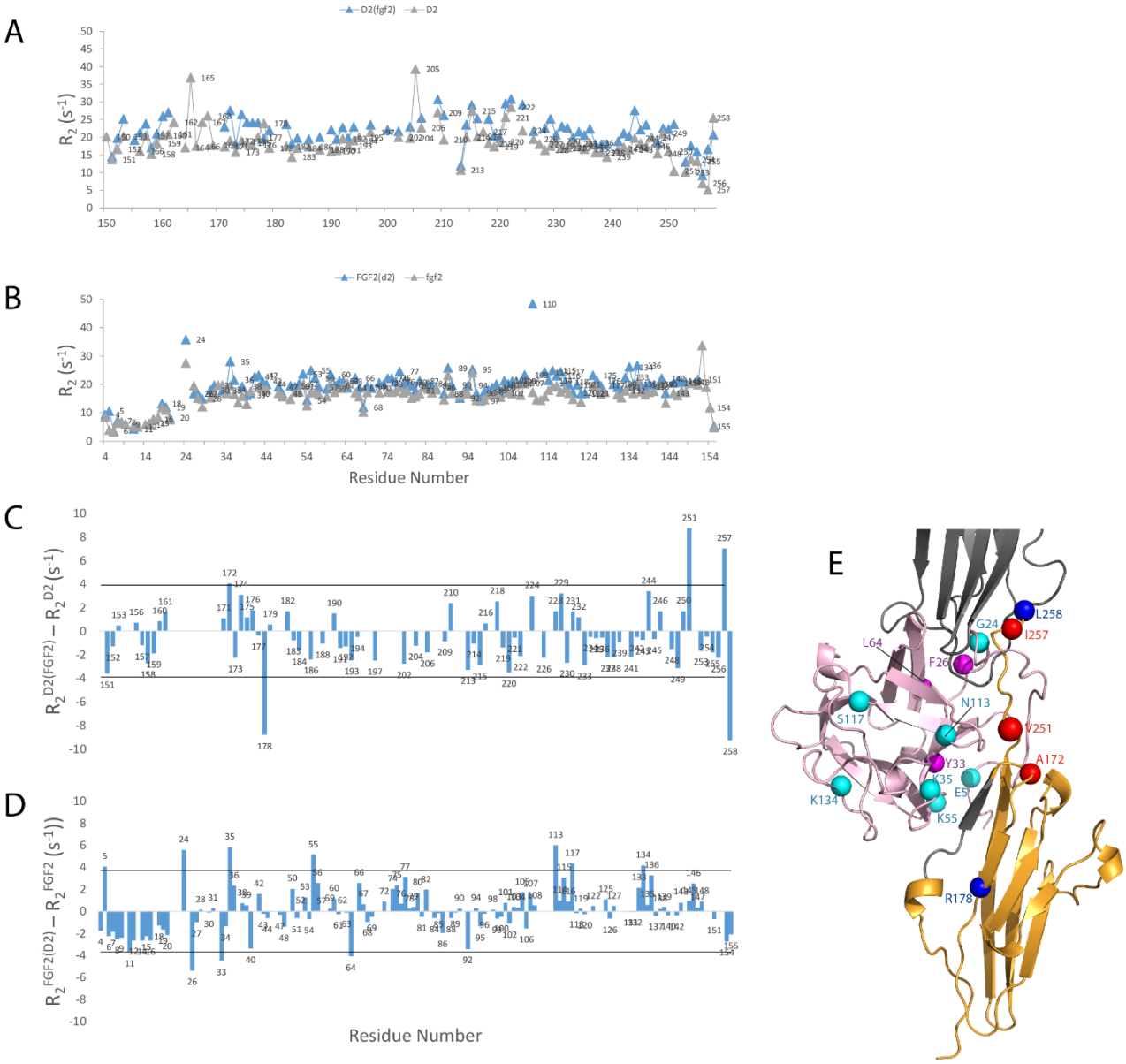

Figure S3. R_2 values measured for FGFR-D2 and FGF2 partners in apo and complexed form.
R_2 for FGFR-D2 (**A**) and FGF2 (**B**) apo (grey) and upon FGFR-D2/FGF2 complex formation (blue) are reported as a function of the residue number. Relaxation experiments were acquired at 600 MHz at ^{15}N-FGF2:^{15}N-FGFR-D2 1:1 stoichiometric ratio. The average transverse relaxation rate values measured for FGFR-D2 apo and FGFR-D2 in complex with FGF2 increases from 18.05±1.78 s^{-1} to 22.54±1.91 s^{-1}. For the FGF2 counterpart the average R_2 values increases from 17.68±0.61 s^{-1} to 20.29±0.57 s^{-1} upon complex formation.
Differences between FGFR-D2 and FGF2 R_2 values in FGFR-D2/FGF2 complex and their apo values are reported in (C) and (D) for FGFR-D2 and FGF2, respectively. Straight lines represent ± ($<|R_2^{FGF2/FGFR-D2}-R_2^{FGFR-D2}|> + 2\sigma$) and ± ($<|R_2^{FGF2/FGFR-D2)}-R_2^{FGF2}|> + 2\sigma$) in (C) and (D), respectively. Significant R_2 variations upon RA addition are plotted on the structures in (E): blue and cyana spheres represent residues that decrease their R_2 value for FGFR-D2 and FGF2, respectively, whereas red and magenta spheres represent residues that increase their R_2 value for FGFR-D2 and FGF2, respectively.

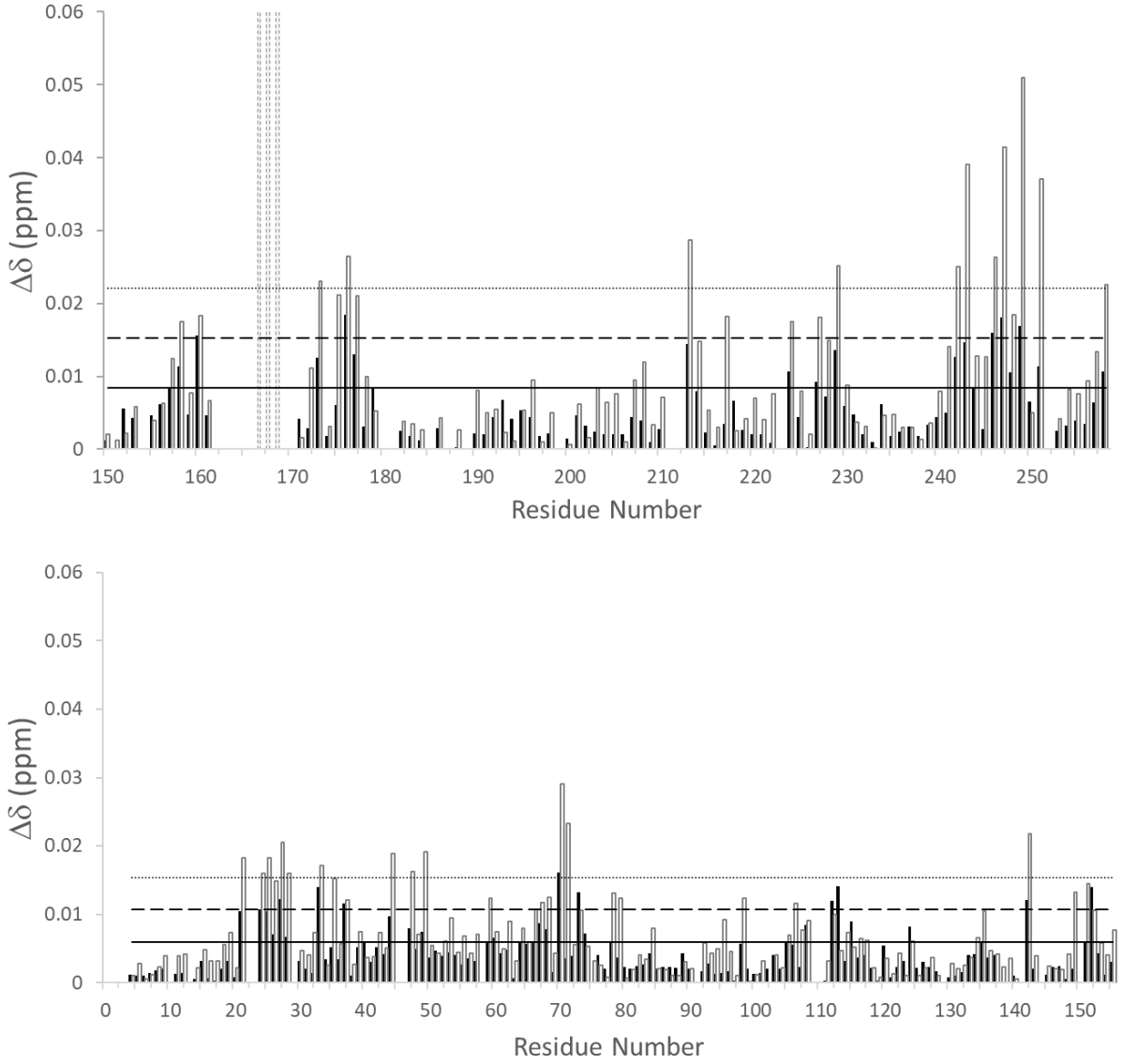

Figure S4. CSP effects on ^{15}N-FGFR-D2/^{15}N FGF2 complex upon RA addition observed for ^{15}N-FGFR-D2:^{15}N FGF2: RA 1:1:5 (black) and ^{15}N-FGFR-D2:^{15}N FGF2: RA 1:1:10 (white) bars. Continuous, dashed, and dotted lines represent the CSP average values (⟨CSP⟩), ⟨CSP⟩ + 1σ, and ⟨CSP⟩ + 2σ, respectively, for the 1:1:10 stoichiometric ratio. Experiments were acquired on 0.26 mM proteins (pH = 6.5, 25 °C) at 600 MHz.

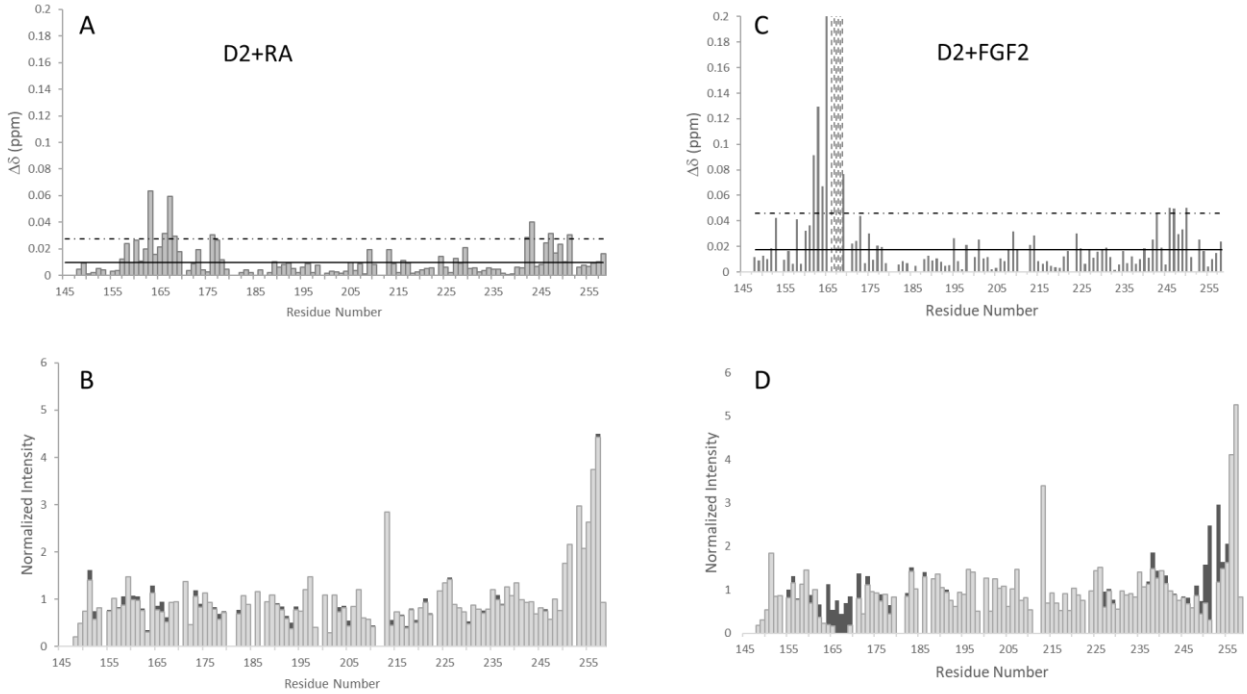

Figure S5 Chemical shift perturbations and cross peak intensity changes for FGFR-D2 upon RA (left) or FGF2 (right) addition at 15N-FGFR-D2:RA 1:5 and 15N-FGFR-D2:FGF2 1:1 molar ratios, respectively. Experiments were acquired at 600 MHz, pH = 6.5, at 25 °C.

Continuous, dashed, and dotted lines represent the CSP average values (⟨CSP⟩), ⟨CSP⟩ + 1σ, and ⟨CSP⟩ + 2σ, respectively. Dashed vertical bars in (C) represent residues whose intensities broaden beyond detection upon complex formation. FGFR-D2 normalized intensities in the absence (black bars) and in the presence (grey bars) of RA (B) or FGF2 (D).

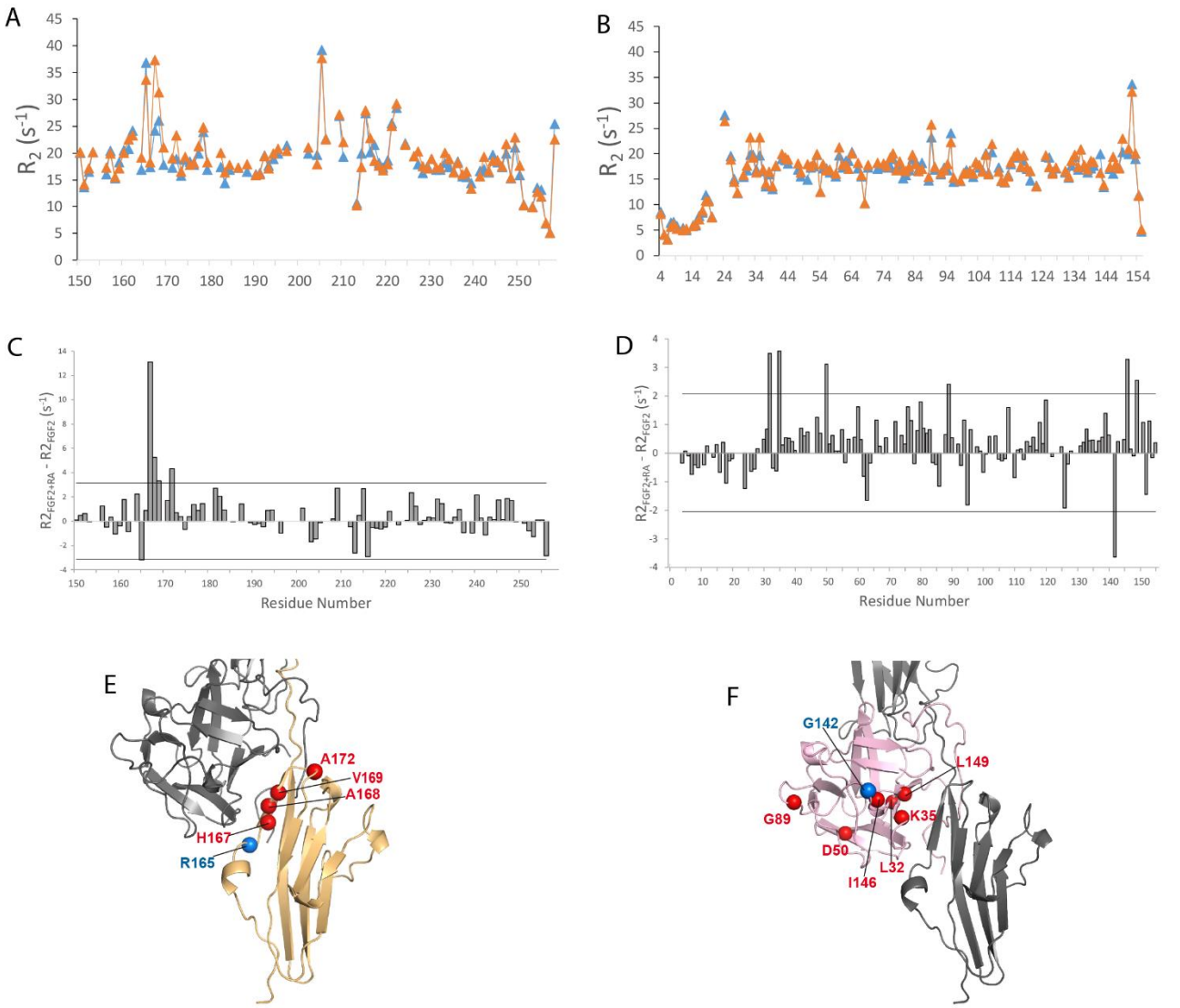

Figure S6. R_2 for FGFR-D2 (A) and FGF2 (B) for apo (blue) and upon RA addition (orange) are reported as a function of the residue number. Stoichiometric ratios were 1:0 and 1:5 for ^{15}N-FGFR-D2:RA, and 1:0 and 1:5 for ^{15}N-FGF2:RA. Experiments were acquired at 600 MHz, pH = 6.5, at 25 °C, at 600 MHz. Differences between protein R_2 values in the presence and in the absence of RA are plotted as a function of residue number for FGFR-D2 (C) and FGF2 (D). Residues exhibiting R_2 increase and decrease upon RA addition are highlighted on FGFR-D2 (E) and FGF2 structures (F) as red and blue spheres, respectively.

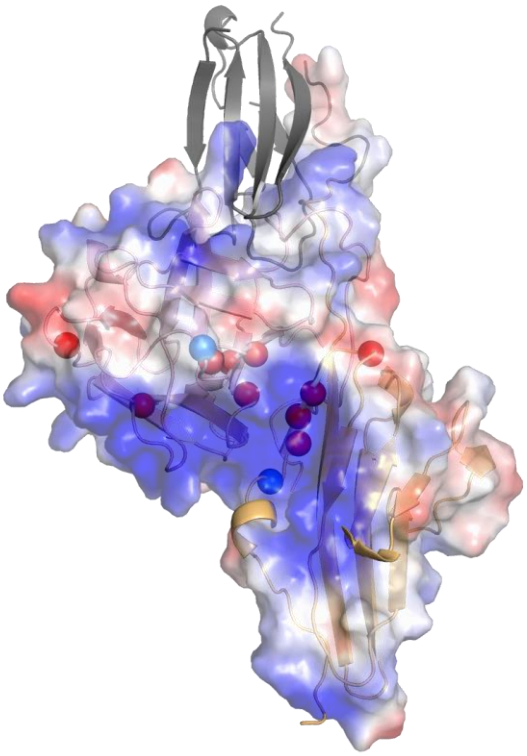

Figure S7. Electrostatic surface of the complex showing the positive canyon (blue) at the interface between FGF2 and FGFR-D2. Spheres are shown and coloured as in Figure S6 E, F.

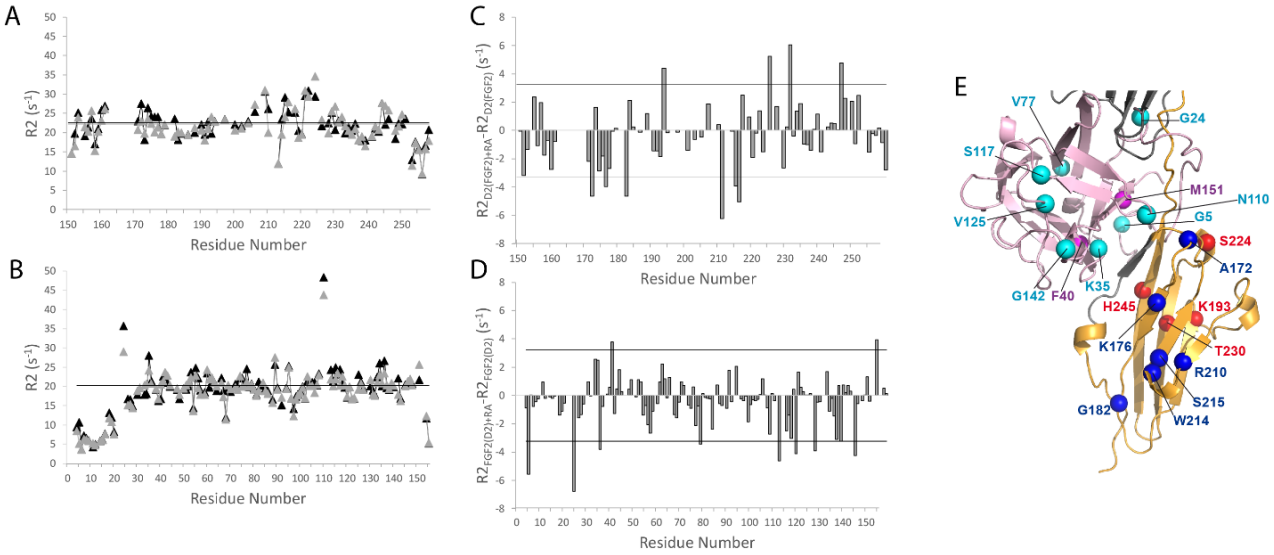

Figure S8. Changes in R_2 values upon RA addition to FGFR-D2/FGF2 complex.
R_2 values for FGFR-D2 (A) and FGF2 (B) in FGFR-D2/FGF2 complex (black triangles) and upon RA addition (grey triangles) are reported as a function of the residue number. Experiments were acquired on 0.26 mM proteins, at 600 MHz at ^{15}N-FGF2:^{15}N-FGFR-D2:RA 1:1:0 and 1:1:5 molar ratios. Samples were dissolved in 30 mM deuterated phosphate buffer, pH = 6.5, at 25 °C. Straight lines indicate the R_2 average value. Differences between FGFR-D2/FGF2 R_2 values and FGFR-D2/FGF2 R_2 upon RA addition are reported in (C) and (D) for FGFR-D2 and FGF2, respectively. Straight lines represent $\pm(<|R_2^{(FGF2/FGFR-D2)+RA} - R_2^{(FGF2/FGFR-D2)}|> +2\sigma)$. Significant R_2 variations upon RA addition are plotted on the structures in (E). Blue and cyana spheres represent residues that decrease their R_2 value for FGFR-D2 and FGF2, respectively, whereas red and magenta spheres represent residues that increase their R_2 value for FGFR-D2 and FGF2, respectively. Signal intensity of 162-170 residues of FGFR-D2 domain broadens beyond detection upon FGF2 binding, and are coloured in grey on the structure.

Altogether, R_2 measurements showed that the addition of RA to the complex was reflected in an increased conformational exchange at the level of the surface including residues located in the βC, βF, βG strands and EF loop and in the stabilisation of residues located on the opposite face comprising βA', βB, βB', βD, βE strands) (Figure S8 A, C, E). As far as FGF2 is concerned, few residues close to the heparin binding site (K35, G142) and to the primary and secondary binding sites (G24, N110) are stabilised upon RA addition (Figure S8 B, D, E). At variance FGF2 residue M151, in contact with FGFR-D2 residue A168 in the X-ray structure [12b], exhibited an increased conformational exchange. It is interesting to note that M151 belongs to a group of few residues whose mutation resulted in a dramatic decrease of binding to the receptor [12a].

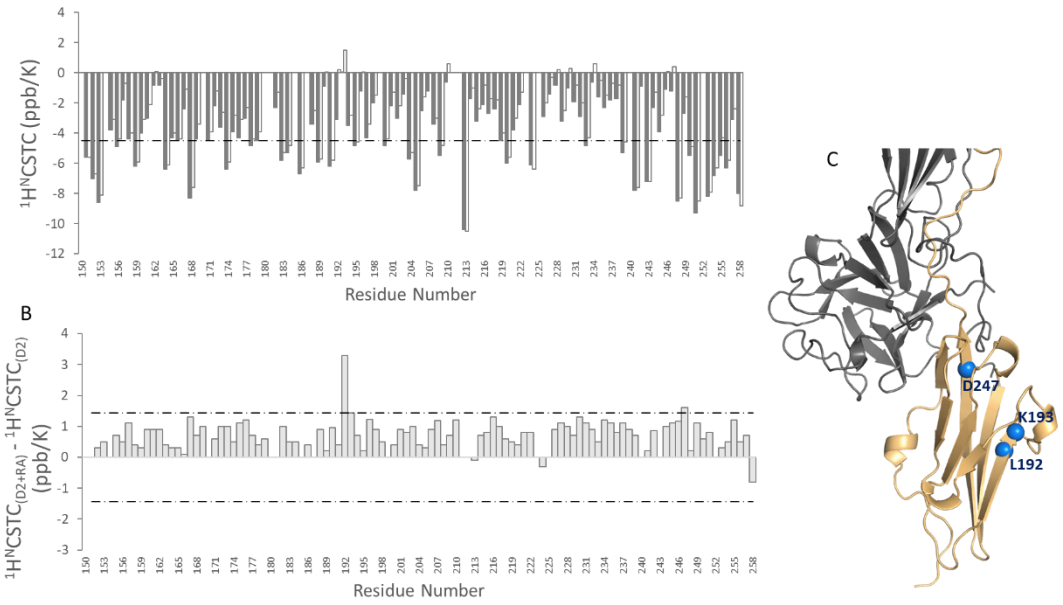

Figure S9. Changes in $^1H^NCSTC$ for FGFR-D2 in the presence of RA. A) Temperature coefficients measured for FGFR-D2 (filled bars) and FGFR-D2+RA (empty bars) at 1:5 stoichiometric ratio. Dashed line for H-bond threshold at -4.5 ppb/K. Coefficients were derived from ^1H-^{15}N-HSQC spectra acquired at 298.2, 301.1, 304.4, 307.7, and 312.1 K. B) Differences between $^1H^NCSTC$ of FGFR-D2+RA and FGFR-D2. Dashed lines indicates the $\pm(<|^1H^NCSTC|> + 2\sigma)$; C) Residues showing differences higher than 2σ from the average are highlighted on the structure as blue spheres.

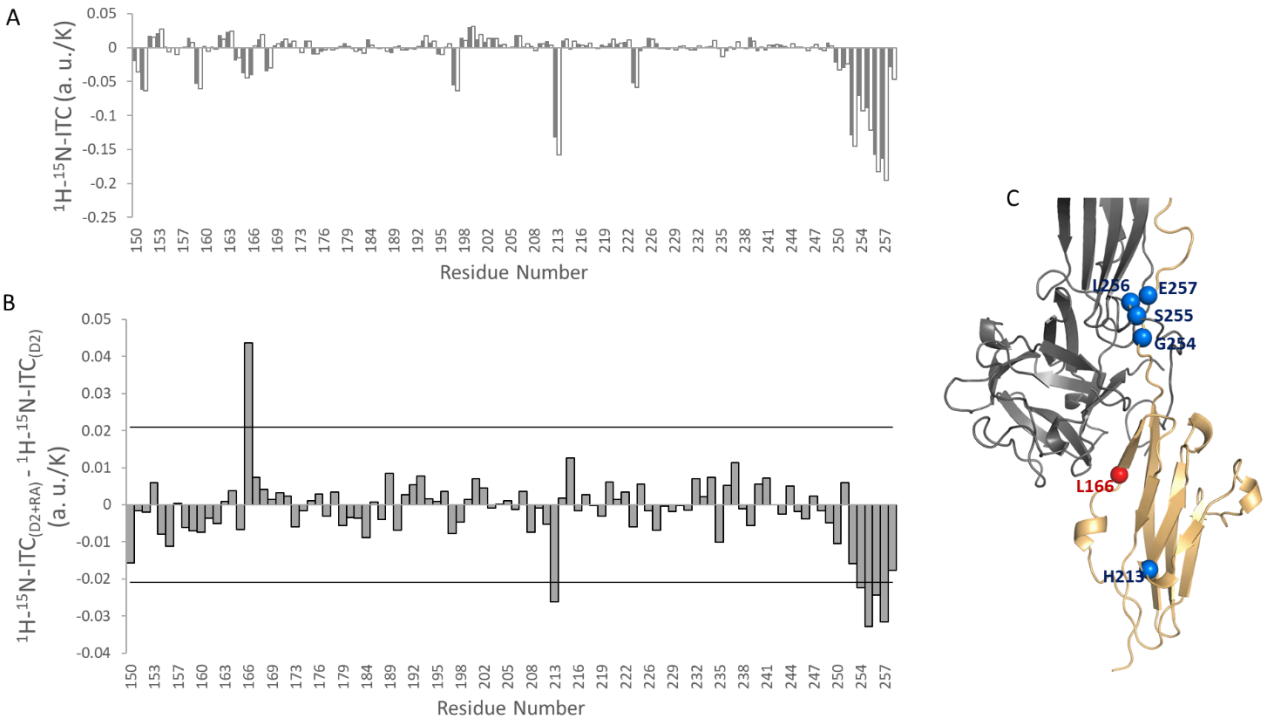

Figure S10. ^{1}H-^{15}N-ITCs for FGFR-D2 in the presence of RA. A) Temperature coefficients measured on FGFR-D2 sample (grey bars) and FGFR-D2+RA (white bars) at 1:5 stoichiometric ratio. Coefficients were derived from ^{1}H-^{15}N-HSQC spectra acquired at 298.2, 301.1, 304.4, 307.7, and 312.1 K. B) Differences between ^{1}H-^{15}N-ITCs of FGFR-D2+RA and FGFR-D2. Straight lines represent the $\pm(\langle|^1\text{H-}^{15}\text{N-ITC}|\rangle + 2\sigma)$; C) Residues showing intensity increase or decrease larger than 2σ from the average are highlighted on the structure as blue and red spheres, respectively.

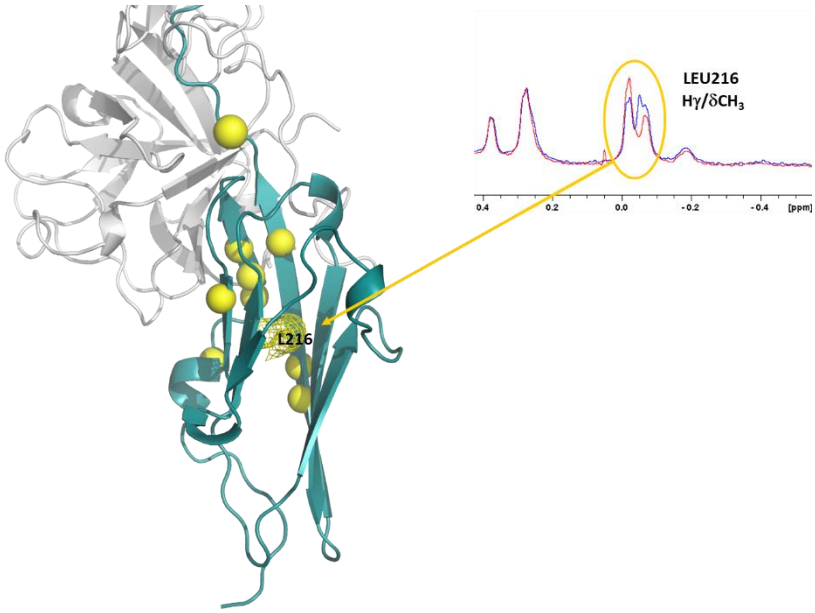

Figure S11. L216 sidechain resonances of FGFR-D2 are shifted upon RA addition. Residues showing CSP higher than (⟨CSP⟩ + 2σ) are highlighted as yellow spheres on the structure of panel. L216 methyl groups are highlighted as grid spheres and labelled. The inset reports the overlap of the high field regions of 1D ^{1}H NMR spectra recorded at 600 MHz for FGFR-D2 domain alone (red) and in the presence of RA (blue).

Amide temperature coefficients highlight long-range perturbations of FGFR-D2 upon FGF2 binding

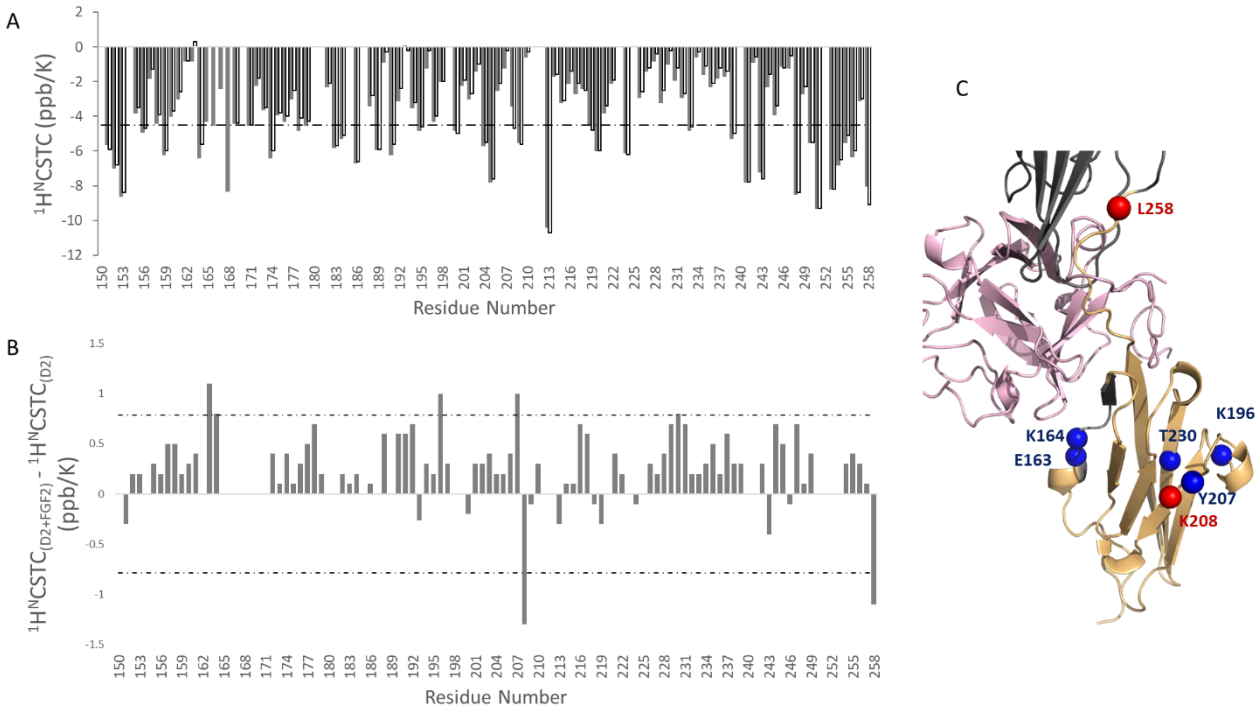

Figure S12. A) Changes in $^1H^N$CSTC for FGFR-D2 in the presence of FGF2. Temperature coefficients measured for FGFR-D2 (grey bars) and FGFR-D2 +FGF2 (white bars) at 1:1 stoichiometric ratio. Dashed line for H-bond threshold at -4.5 ppb/K. Coefficients were derived from ^1H-^{15}N-HSQC spectra acquired at 298.2, 301.1, 304.4, 307.7, and 312.1 K. B) Differences between $^1H^N$CSTC of FGFR-D2+FGF2 and FGFR-D2. Dashed lines represent ± (<|$^1H^N$CSTC|> + 2σ). C) Residues showing significant variations are highlighted on the structure as red and blue spheres for increased and decreased $^1H^N$CSTC's, respectively.

The histogram of $^1H^N$CSTCs, as a function of residue number, indicated a general decrease of the coefficients, consistent with a higher protection from exchange (Figure S12). The stiffening of FGFR-D2 backbone upon FGF2 binding was especially marked for residues at the primary binding site (E163, K164), and in βC' (K196), βD (Y207) and βF (T230) strands (blue spheres, Figure 7C). Only few residues, namely K208 and H258, showed an increase of disorder upon complexation (red spheres, Figure 7C).

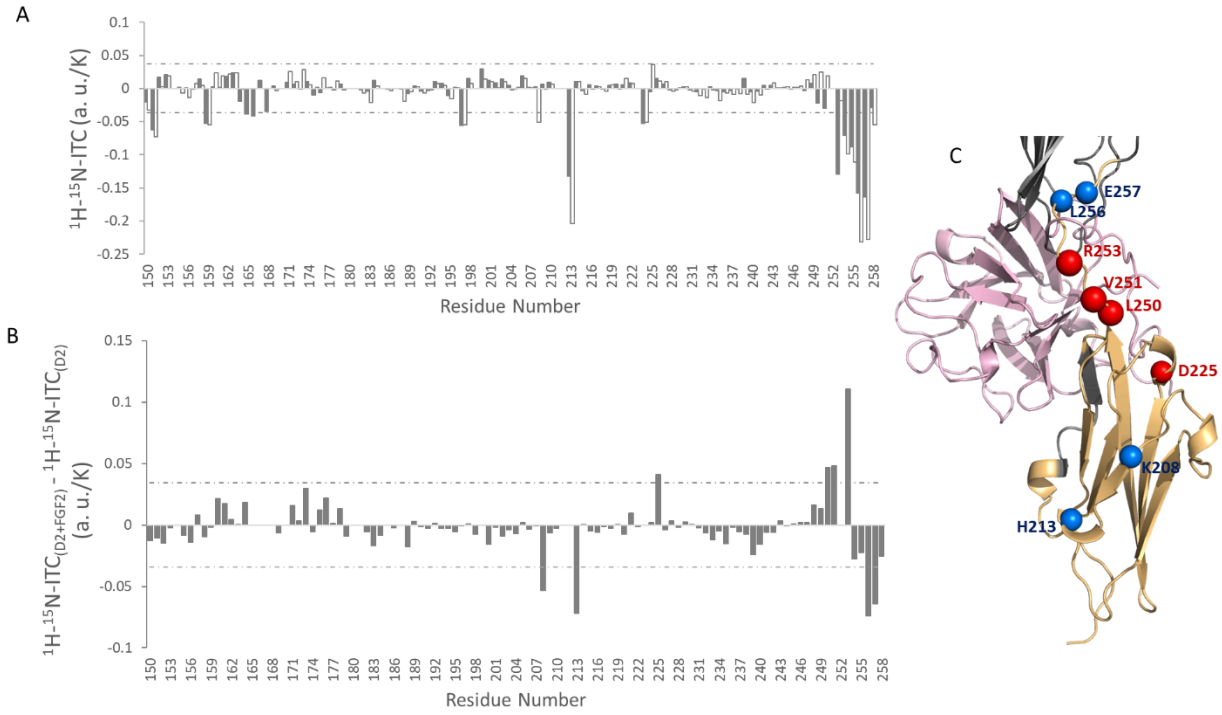

Figure S13. A) ^{1}H-^{15}N-ITC of FGFR-D2 alone (grey bars) and for the complex with FGF2 (white bars) at 1:1 stoichiometric ratio. Coefficients were derived from ^{1}H-^{15}N-HSQC spectra acquired at 298.2, 301.1, 304.4, 307.7, and 312.1 K B) ^{1}H-^{15}N-ITC differences between FGFR-D2/FGF2 and FGFR-D2 apo. Dashed lines represent ±(<|^{1}H-^{15}N-ITC |> + 2σ). C) Significant ^{1}H-^{15}N-ITC variations are shown on FGFR-D2 structure as red and blue spheres for increased and decreased ^{1}H-^{15}N-ITC's, respectively.

^{1}H-^{15}N-ITCs coefficients showed that residues at the binding interface (K164, R165, V169) became broader in the complex, moving towards an intermediate exchange regime and paralleling the behavior of the 166-168 CAM motif (Figure S13). In the presence of FGF2, a few residues of the entire C-terminal region (248-253) exhibited a decreased contribution of exchange, which reflects the stabilization of this primary interaction site. At variance, distal regions (K208, H213) showed an increased R_{ex} contribution upon FGF2 binding (red spheres, Figure 7D). The same behaviour was observed for residues L256 and E257, suggesting that the addition of FGF2 is unable to stabilize a single conformation of the FGFR-D2-D3 linker region.

Table S1 Ambiguous interaction restraints (AIR) defined for FGF2 and FGFR-D2

FGFR-D2	
Active	162, 163, 164, 165, 166, 167, 168, 169, 171, 227, 243, 246, 247, 249, 250, 251, 253.
Passive	159, 160, 161, 170, 172, 173, 176, 223, 226, 228, 230, 241, 242, 245, 252, 254.
FGF2	
Active	32, 33, 34, 35, 36, 37, 40, 109, 110, 112, 113, 115, 149, 152
Passive	31, 53, 107, 108, 111, 127, 129, 144, 147, 151.

Table S2 Statistics of the top four HADDOCK score best ranked clusters of FGF/FGFR-D2 docking simulation.

	Cluster 2 (most reliable)	Cluster 1 (2^{nd})	Cluster 4 (3^{rd})	Cluster 3 (4^{th})
HADDOCK Score (a.u.)	-121.8 ± 7.5	-95.1 ± 3.3	-92.8 ± 12.1	-83.4 ± 7.0
Cluster Size[a]	8	10	8	8
RMSD-Emin[b] ($kcal \cdot mol^{-1}$)	0.77± 0.44	16.53±0.11	17.78±0.14	17.25±0.11
Van der Waals Energy ($kcal \cdot mol^{-1}$)	-51.96±8.50	-38.09±1.94	-42.60±4.46	-34.36±6.67
Intermolecular Energy[c] ($kcal \cdot mol^{-1}$)	-353.10±29.20	-241.30±37.62	-250.21±29.84	-244.96±24.33
Desolvation Energy[d] ($kcal \cdot mol^{-1}$)	-8.99±4.23	-13.88±6.22	-6.84±11.09	-5.77±3.25
Buried Surface Area ($Å^2$)	1716.60±110.69	1545.86±84.94	1399.03±34.86	1438.59±84.45

[a]Number of structures in a given cluster.
[b]Overall backbone RMSD from the lowest energy structure.
[c]The intermolecular energies ($kcal\ mol^{-1}$) were calculated with the OPLS force field parameters for non-bonded atoms.
[d]The desolvatation energy ($kcal\ mol^{-1}$) was calculated using the atomic desolvation parameters by Fernandez-Recio et al. (Fernandez-Recio, J., Totrov, M., and Abagyan, R. (2004) Journal of Molecular Biology 335, 843-865).

Table S3 Ambiguous interaction restraints (AIR) defined for FGFR-D2

FGFR-D2	
Active	163, 166, 167, 168, 176, 242, 243, 247, 251
Passive	156, 159, 160, 162, 161, 164, 165, 169, 170, 174, 175, 177, 178, 213, 215, 217, 226, 228, 230, 241, 244, 245, 248, 249, 250,252, 253

Table S4 Statistics of the top four HADDOCK score best ranked clusters of FGFR-D2/RA docking simulation.

	Cluster 1 (most reliable)	Cluster 2 (2^{nd})	Cluster 3 (3^{rd})	Cluster 5 (4^{th})
HADDOCK Score (a.u.)	-2.98±2.27	1.42±5.2	6.22±2.09	7.38±4.5
Cluster Size[a]	123	32	12	5
RMSD-Emin[b] ($kcal \cdot mol^{-1}$)	0.41±0.24	0.60±0.05	0.52±0.04	0.56±0.02
Van der Waals Energy ($kcal \cdot mol^{-1}$)	0.48±0.22	0.62±0.17	0.85±0.43	0.73±0.71
Intermolecular Energy[c] ($kcal \cdot mol^{-1}$)	1.44±0.40	2.79±1.13	2.77±1.47	2.4±0.83
Desolvation Energy[d] ($kcal \cdot mol^{-1}$)	-4.42±2.42	-1.36±4.74	3.45±2.89	4.98±4.63
Buried Surface Area ($Å^2$)	436.01±27.49	461.22±33.11	481.02±15.22	411.43±38.59

[a]Number of structures in a given cluster.
[b]Overall backbone RMSD from the lowest energy structure.
[c]The intermolecular energies ($kcal\ mol^{-1}$) were calculated with the OPLS force field parameters for non-bonded atoms.
[d]The desolvatation energy ($kcal\ mol^{-1}$) was calculated using the atomic desolvation parameters by Fernandez-Recio et al. (Fernandez-Recio, J., Totrov, M., and Abagyan, R. (2004) Journal of Molecular Biology 335, 843-865).